Clays Clay Miner., Vol. 70, No. 3:370–385, 2022
https://doi.org/10.1007/s42860-022-00194-5

ORIGINAL PAPER

A Density Functional Theory (DFT) Investigation of Sulfur-Based Adsorbate Interactions on Alumina and Calcite Surfaces

Stanley Ou · Jessica E. Heimann · Joseph W. Bennett

Accepted: 24 June 2022
© The Author(s), under exclusive licence to The Clay Minerals Society 2022

Abstract With fossil-fuel consumption at an all-time high, air pollution is becoming one of the most prominent problems of the 21st century. In addition to their devastating effects on the environment, sulfur-based pollutants are problematic for infrastructure by undermining the structural stability of various oxide-based surfaces found in clays and clay minerals. Calcite ($CaCO_3$) and alumina (α-Al_2O_3) are two such mineral oxides with surfaces that are potentially susceptible to damage by sulfur-based adsorbates. Their surface interactions with a wide range of sulfur-based pollutants, however, have yet to be studied adequately at the atomistic level. This problem can be addressed by utilizing density functional theory (DFT) to provide molecular-level insights into the adsorption effects of H_2S, SO_2, SO_3, H_2SO_3, and H_2SO_4 molecules on calcite and alumina surfaces. DFT can be used to compare different types of adsorption events and their corresponding changes in the geometry and coordination of the adsorbates, as well as delineate any possible mineral-surface reconstructions. The hypothesis driving this comparative study was that the mineral-oxide surface structure will dictate the surface adsorption reactivity, i.e. the flat carbonate unit in calcite will behave differently from the Al–O octahedra in alumina under both vacuum and hydrated surface conditions. The set of sulfur-based adsorbates tested here exhibited a wide range of interactions with alumina and fewer with calcite surfaces. Events such as hydrogen bonding, sulfate formation, atom abstraction, and the formation of surface water groups were more prevalent in alumina than calcite and were found to be dependent on the surface termination. The results of this work will prove instrumental in the design of clay and mineral-based materials resilient to sulfur-based pollutants for use in construction and infrastructure such as smart building coatings and anti-fouling desalination membranes, as DFT methods can garner the atomistic insights into mineral-surface reactivity necessary to unlock these transformative technologies.

Keywords DFT + thermodynamics · Atomistic modeling · Mineral-surface transformations · Surface-adsorption reactivity

S. Ou
Montgomery Blair High School, Silver Spring, MD 20901, USA

S. Ou · J. E. Heimann · J. W. Bennett (✉)
Department of Chemistry and Biochemistry, University of Maryland Baltimore County, Baltimore, Maryland 21250, USA
e-mail: bennettj@umbc.edu

Introduction

Air pollution from global fossil-fuel consumption has been linked to serious health issues and other negative effects in modern societies (Martins et al., 2019; Perera, 2017). Previous studies on the impact of air pollution in cities focused on the interplay of modeling, sustainability, and energy planning. One topic that is not as prevalent, however, is the deleterious effects of small-molecule pollutants on clays and clay mineral-based

https://doi.org/10.1007/s42860-022-00194-5 Published online by Cambridge University Press

building and construction materials (Bridges et al., 2015; Gulia et al., 2015). The more notorious molecules such as NO_x and CO_2 (Fenger, 1999; Hosseinabad & Moraga, 2017) have received much attention, as have building sensors for particulate matter (Garcia-Florentino et al., 2020; Lim et al., 2019), but few studies focus on the atomistic interactions that happen at the interface of sulfur-containing small molecules and oxide surfaces present on or in buildings and structures (Summers, 1979; Zheng et al., 2019).

Sulfur-based air pollutants such as SO_2 and H_2S are common byproducts of fossil-fuel combustion and are present in urban and industrial areas (Fenger, 1999; Garcia-Florentino et al., 2020). As a main group element with a wide array of oxidation states ranging from –2 in H_2S to +6 in SO_3, the sulfur center in these pollutants poses a unique threat. The reactivity of sulfur is dictated by its oxidation state and surrounding chemical environment, specifically in surface-adsorption interactions (Shannon & Prewitt, 1969). As such, sulfur adsorbate geometries are highly variable and linked to changes in surface terminations, molecular symmetry, and hydration sphere. Also worth noting is that sulfur compounds can undergo redox reactions, with changes in charge, size, and shape correlated to changes in the electronic state. For example, atmospheric SO_2 (bent) can form SO_3 (trigonal planar) through a variety of means such as catalytic oxidation on the surface of traffic-related black carbon or photooxidation by hydroxyl radicals (Yao et al., 2020). Similarly, SO_3 is a crucial component in the formation of H_2SO_4 (tetrahedral), the main component of acid rain. In addition to the devastating environmental consequences, sulfur-based pollutants also pose challenges to the oxide-based materials used in architecture such as limestone, bricks, and cement (Bravo et al., 2006; Graue et al., 2013).

Previous studies have shown that oxide-based materials are particularly vulnerable to sulfur-based pollutants. For example, there is evidence of SO_3^{2-} and SO_4^{2-} formation when hematite (Fe_2O_3) surfaces are exposed to SO_2 (Baltrusaitis et al., 2007). Interactions of similar or greater strength have been observed across a variety of oxide surfaces including TiO_2, FeOOH, MgO, Na_2O, K_2O, CaO, $Ca(OH)_2$, and Na_2SO_3 (Baltrusaitis et al., 2007, 2010; Galloway et al., 2015; He et al., 2019, 2020; Schneider et al., 2001). These bonding events are disruptive to the surfaces, as adhesion causes local changes in the surface structure that, over time, could cause the material to deteriorate, become brittle, and crack. On a larger scale, such interactions may permeate below the surface, hinder architectural stability, and, in a worst-case scenario, may be partially responsible for structural damage and subsequent building collapse.

Alumina (α-Al_2O_3) and calcite ($CaCO_3$) are two minerals that are potentially prone to such consequences, as they are components of construction materials such as brick and limestone, respectively. Previous work showed that interactions with sulfur-containing adsorbates will cause significant changes to alumina surfaces and aluminum oxide-based nanoparticles, effectively capturing small-molecule adsorbates (Abbaspour-Tamijani et al., 2020; Bennett et al., 2017; Bjorklund et al., 2019). Sulfur-based adsorbates are also responsible for the degradation of $CaCO_3$, forming the more brittle mineral gypsum ($CaSO_4{\cdot}2H_2O$), as the ratio of sulfate to carbonate anions increases at the surface (Coccato et al., 2017; Gettens et al., 1974). A mix of carbonate and sulfate ions are also key components in the films that develop on the surface of desalination membranes, linking the degradation mechanisms of these two disparate technologies. Other calcium-based oxides such as CaO and $Ca(OH)_2$ have shown potential in capturing SO_2 and SO_3, suggesting that $CaCO_3$ may respond similarly to a variety of sulfur-based small-molecule adsorbates (Galloway et al., 2015). However, to the best of the authors' knowledge, no comparative analysis of the interactions between sulfur-based adsorbates and alumina and calcite (001) surfaces that details changes in geometry on an atomistic level has yet been done, let alone for multiple surface terminations that can occur over a wide range of chemical environments. Understanding these atomistic interactions on alumina and calcite is important to prevent potentially deleterious surface reactions and their subsequent macroscale transformations.

The present comparative study was driven by the hypothesis that the mineral oxide surface structure will dictate the surface adsorption reactivity, i.e. the flat carbonate unit in calcite will behave differently from the Al–O octahedra in alumina under both vacuum and hydrated surface conditions. In this work, density functional theory (DFT), a quantum-based modeling method designed to investigate the electronic structure of a many-body system, was employed. DFT can be used to compare different types of adsorption events and their corresponding changes in the geometry and coordination of the adsorbates, as well as delineate any possible mineral-surface reconstructions. In recent years, DFT

https://doi.org/10.1007/s42860-022-00194-5 Published online by Cambridge University Press

has become a widely used tool in delineating structure-adsorbate interactions due to its accessibility and efficiency (Bennett et al., 2017; Burke, 2012; Kohn & Sham, 1965). The atomistic data obtained from DFT, which includes the number and types of bonds that are created or broken and any changes in bond length and coordination, can be used to determine the relative stability of various oxide surfaces in the presence of sulfur-containing adsorbates. The objective of this study was to understand how sulfur-containing adsorbates interact with mineral oxides by finding evidence of proton abstraction, hydrogen bonding, and covalent bonding across the various mineral surfaces and their different terminations. The results here suggest both that: (1) adsorbate–surface interactions are stronger on clay-mineral surfaces with exposed metal atoms than on hydrated surfaces; and (2) adsorption is stronger on alumina surfaces than on calcite surfaces, as the flat carbonate unit prevents adsorbates from reacting with subsurface Ca cations.

Materials and Methods

Computational Parameters

All calculations in this study employed periodic DFT methods as implemented in *Quantum ESPRESSO*, an open-source software used to compute electronic and material structures at the nanoscale (Giannozzi et al., 2009). The computational parameters described here are consistent with recent studies that probe surface–adsorbate interactions (Bennett et al., 2020; Grimes et al., 2021; Heimann et al., 2021). All atoms were represented using the well-vetted Garrity Bennett Rabe Vanderbilt (GBRV)-type ultrasoft pseudopotentials (Garrity et al., 2014). A plane-wave cutoff of 40 Ry and charge density cutoff of 320 Ry was used for all relaxations. For the bulk structure relaxations, a 6×6×6 k-point grid was employed, and the convergence criteria for self-consistent relaxation calculations was 5×10^{-6} eV. All calculations were performed at the GGA level using the Wu-Cohen (WC)-modified PBE-GGA exchange correlational constant for solids (Wu & Cohen, 2006). All structures were visualized in *XCrySDen*, an open-source visualization program for crystalline and molecular structures (Kokalj, 1999). The bond lengths, lattice parameters, and observed surface–adsorbate interactions were collected through *XcrySDen* visualizations. All cell parameters are presented in Section S1 of the Supplemental Materials.

Bulk Crystal Structures

Both the alumina and calcite bulk structures were obtained from the Inorganic Crystal Structure Database (ICSD) (Hellenbrandt, 2004). Bulk alumina (Fig. 1a) consists of 30 atoms and contains six formula units in its hexagonal unit cell. The experimental lattice parameters are as follows: a = 4.759 Å, b = 4.759 Å, c = 12.993 Å, α = 90°, ß = 90°, and γ = 120°. The Wyckoff positions are designated as Al (12c; 0, 0, 0.352) and O (18e; 0.306, 0, 0.250) (Toebbens et al., 2001). The bulk calcite structure (Fig. 1b) also features 30 atoms and six formula units in a hexagonal unit cell. The experimentally determined bulk lattice parameters for calcite are as follows: a = 4.999 Å, b = 4.999 Å, c = 16.914 Å, α = 90°, ß = 90°, and γ = 120°. The Wyckoff positions for calcite are Ca (6b; 0, 0, 0), C (6a; 0, 0, 0.250), and O (18e; 0.257, 0, 0.250) (Chessin et al., 1965). In each structure, the cation (Al or Ca) is octahedrally bound to a series of oxygen anions. The bulk structures were fully relaxed, with no fixed atoms, to ensure that the lattice parameters and bond lengths calculated in this work correlate with experimental and previously computed data within 1% (Gunasekaran & Anbalagan, 2007; Liu et al., 2009). After ensuring the calculations were representative of the known materials, the bulk structures were used to generate 2×2×1 supercell slabs of both alumina and calcite for use in surface–adsorbate calculations.

Surface Slab Generation

Using the relaxed bulk structures, 2×2×1 supercells were created and then cleaved along the (001) direction. The surfaces were cleaved to expose either Al or Ca metals as the surface terminating layer. Each side of the surface slab had one half of an inversion symmetric monolayer exposed, along the diagonal of the hexagonal cell, to maintain charge neutrality across the height of the surface slab. This was consistent with previously published surface slab generation methodology (Corum et al., 2017; Huang et al., 2017). These surface slabs contained at least 15 Å of vacuum along the (001) direction, specifically 15.02 and 17.38 Å for Al_2O_3 and $CaCO_3$, respectively, to prevent the surfaces from interacting with each other. The difference in the

https://doi.org/10.1007/s42860-022-00194-5 Published online by Cambridge University Press

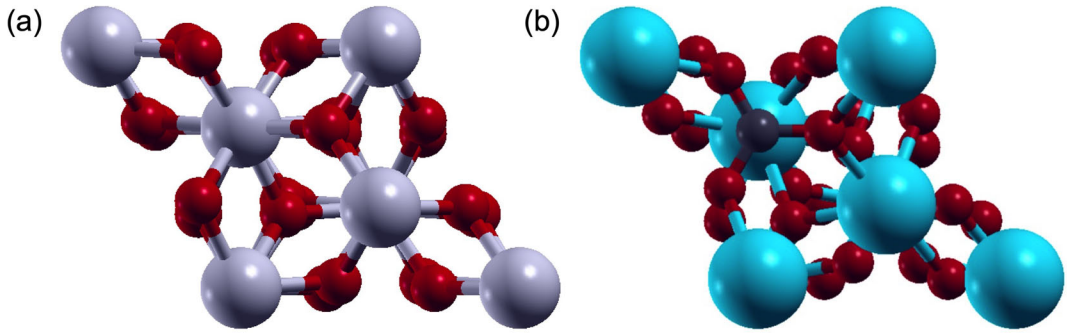

Fig. 1 The bulk structures of: **a** alumina and **b** calcite viewed along the (001) axis to show the similarities between the two hexagonal structures. Aluminum, oxygen, calcium, and carbon are represented as gray, red, blue, and black spheres, respectively

amount of vacuum arose due to the different out-of-plane lattice parameters of Al_2O_3 and $CaCO_3$. The surface slabs were allowed to relax fully, with no fixed layers or atoms, before being used in the surface–adsorbate calculations (see below). Surface reconstructions (pre-adsorbate) occurred in both cases; the metal surface half-monolayer relaxed into the first anion (oxide or carbonate) sublayer, in line with results on related systems (Corum et al., 2017). The *k*-point sampling used for all 2×2×1 surface and surface–adsorbate calculations was a 3×3×1 *k*-point set.

Surface Adsorption Events

For the alumina and calcite surfaces, both metal and proton-terminated surfaces were fully relaxed before any adsorbates were introduced. Metal-terminated surfaces are present in ultra-high vacuum, while protonated surfaces are representative models of surface terminations under ambient conditions that result from a surface being exposed to humidity (Huang et al., 2017). The substitution of H for exposed surface metals Al or Ca was intended to probe the adsorption reactivity of surfaces with a layer of water dissociation products present, in lieu of adding explicit water molecules. The H-terminated surfaces were created by exchanging the surface metal cations for protons and balancing the charge. A total of 12 hydrogen atoms (replacing 4 Al^{3+} atoms in the 2×2×1 supercell surface slab) were present on each exposed alumina surface and 4 hydrogen atoms (replacing 2 Ca^{2+} atoms in the 2×2×1 supercell surface slab) were present on each exposed calcite surface. The exchange of surface metals for protons under humid conditions has been shown previously to be favorable, with negative ΔG values for alumina (Abbaspour-Tamijani et al., 2020), delafossite (Huang et al., 2017), and cerussite (Grimes et al., 2021). Here the exchanges were also favorable; ΔG of exchange at pH 5 was –0.55 eV (12 H per side) and –0.92 eV (4 H per side) per proton for alumina and calcite, respectively. A detailed description of the DFT + Solvent Ion method used to obtain these numbers is provided in Section S4 of the Supplemental Materials, as is a plot of ΔG vs pH for both surface exchanges.

The orientation and location of the surface hydrogen atoms also maintain the inversion symmetry of the bulk crystal structures. This reductionist approach to modeling surface states investigates adsorption events on a hydrated surface without adding explicit water, which allows for the determination of adsorption strengths in ultrahigh vacuum conditions and the creation of a baseline set of surface interaction behaviors before increasing the scale and complexity of adsorption studies. Here the focus was on modeling adsorption events with no surface water molecules present. Because no water molecules are displaced, this type of adsorption is typically referred to as outer sphere and is the first type of interaction that an adsorbate will have with a surface. According to the Eigen-Wilkins associative substitution mechanism, outer sphere adsorption can proceed to an inner sphere mechanism, with or without surface waters or water products on the surface (Wilkins, 1991).

To investigate how orientation affects surface–adsorbate interactions, two to four configurations of each pollutant were modeled. The initial adsorbate geometries of H_2S, SO_2, and H_2SO_3 started with the central S directly over (a) a surface metal or (b) an oxygen hollow site, resulting in two different configurations. The planar SO_3 molecule was also initialized in these positions, in both parallel and perpendicular orientations (relative to the surface), resulting in four different starting orientations. Finally, H_2SO_4 was

https://doi.org/10.1007/s42860-022-00194-5 Published online by Cambridge University Press

initialized in a similar manner, but with protons parallel or perpendicular to the surface. What would have been the fourth configuration of H_2SO_4 relaxed to the first configuration, so it was excluded from the analysis. In total, this resulted in 13 DFT calculations for each of the four unique surface types or 52 entries overall. In the present study, these orientations are referred to by the adsorbate name followed by the corresponding number (e.g. the second adsorption configuration of H_2S is H_2S-2). Images of the resulting atomistic relaxations for alumina and calcite are included in Sections S2 and S3, respectively, of the Supplemental Materials. Specifically, the adsorption events on the Al-terminated Al_2O_3 surface are shown in Section S2.1 (Table S2) and in Section S2.2 (Table S3) for the H-terminated Al_2O_3 surface. The adsorption events on the Ca-terminated $CaCO_3$ surface are shown in Section S3.1 (Table S4) and in Section S3.2 (Table S5) for the H-terminated $CaCO_3$ surface.

To quantify the strength of each surface–adsorbate interaction, the adsorption energy E_{ads} was calculated using the following equation:

$$E_{ads} = E_{system} - (E_{adsorbate} + E_{surface})$$

where E_{system} was the energy of the relaxed structure with both the surface and adsorbate present, $E_{adsorbate}$ was the energy of the adsorbate in isolation, and $E_{surface}$ was the energy of the surface on its own. The more negative the calculated adsorption energy, the stronger the surface–adsorbate interaction.

Results

Alumina (α-Al_2O_3)

Using the bulk alumina structure shown in Fig. 1, a 2×2×1 periodic surface slab was generated and used in the surface–adsorbate calculations. The 2×2×1 surface slab structure was found to be sufficiently large to accommodate the varying sizes of the adsorbates in the test set. The Al-terminated alumina surface slab contains 120 atoms with aluminum–oxygen bonds ranging from 1.90 to 2.15 Å in length. Figure 2 compares a top-down view (along the (001) axis) and side view of the in-plane Al-terminated surface structure. As seen in Fig. 2b, the fully relaxed alumina surface structure features layering between the oxygen and aluminum, where each Al cation is located in the center of an octahedron of oxygen atoms. Surface Al atoms relaxed inward, in agreement with similar DFT-based models (Corum et al., 2017). The H-terminated alumina surface consisted of 136 atoms and differs slightly in electronic structure due to the introduction of hydrogen atoms on the surface. Images of this surface are provided in Fig. S1 of the Supplemental Materials.

Al-terminated α-Al_2O_3

For the Al-terminated alumina surface, all configurations of H_2S and SO_2 resulted in moderately strong interactions (depicted in Table S2 of Supplemental Materials) with adsorption energies ranging from –1.65 eV to –2.10 eV (Table 1). In H_2S-2, a surface oxygen was able to deprotonate the adsorbate, producing a protonated oxygen (i.e. surface hydroxyl group) and a thiol group bonded with the surface. Similarly, SO_2 formed $Al_{surface}$–$O_{adsorbate}$ bonds to the surface, as indicated by the bond lengths reported in Table 1. For configurations of SO_3, H_2SO_3, and H_2SO_4, the bonding interactions with the surface were much stronger, with adsorption energies ranging from –3.49 eV to –5.13 eV. An outlier to this trend was SO_3-1, which did not interact much with the surface (E_{ads} = –0.93 eV). The hypothesis was that this is probably due to the lack of contact between the adsorbate and surface in this particular orientation. Due to the +6 oxidation state of the sulfur atom in SO_3, the sulfur center exhibited strong interactions with surface oxygens in all other configurations of SO_3. In fact, a new $S_{adsorbate}$–$O_{surface}$ bond was formed, generating a surface SO_4 unit. This process is potentially harmful to alumina surfaces, as the strength of the interactions suggests that it is practically impossible to uproot the newly formed SO_4 from the Al-terminated surface without significantly damaging the surface structure.

H_2SO_3 and H_2SO_4 exhibited the most negative adsorption energies in the test set. For all configurations of these two adsorbates, the large negative adsorption energies calculated can be explained by a surface oxygen abstracting an H^+ from the adsorbate. It should be emphasized that all configurations of H_2SO_3 and H_2SO_4 tested were deprotonated by the Al-terminated alumina surface, suggesting that this interaction will occur regardless of the orientation of the pollutant. Although H_2SO_3 and H_2SO_4 displayed the strongest surface–adsorbate interactions, all adsorbates tested here have the potential to be detrimental to the Al-terminated

https://doi.org/10.1007/s42860-022-00194-5 Published online by Cambridge University Press

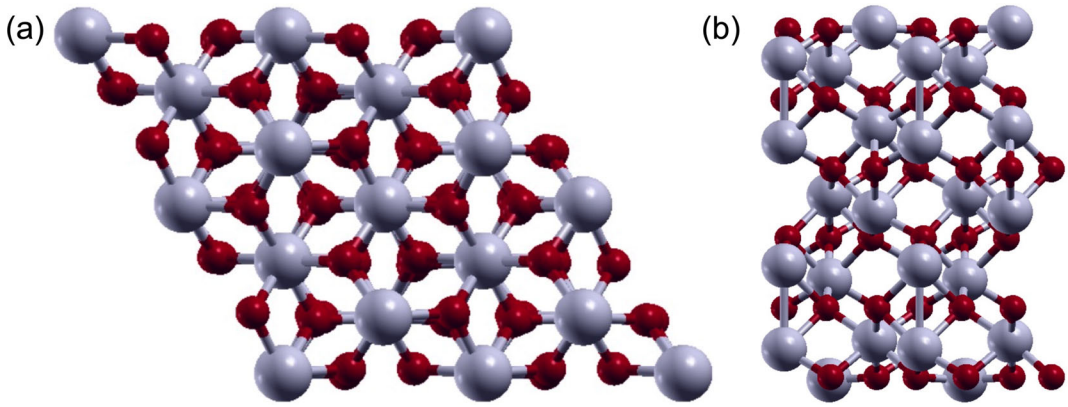

Fig. 2. **a** Top-down view along the 001 axis and **b** side view of the 2×2×1 alumina surface slab. Aluminum and oxygen atoms are represented as gray and red spheres, respectively

alumina surface, as evidenced by their wide range of negative adsorption energies.

H-terminated α-Al_2O_3

When compared to the Al-terminated alumina surface, the H-terminated alumina surface exhibited noticeably weaker surface–adsorbate interactions. As seen in Table 2, H_2S, SO_2, and two configurations of SO_3 interacted weakly with the alumina surface, as only a few hydrogen bonds were present. This resulted in adsorption energies ranging from –0.08 to –1.78 eV. SO_3-3 and SO_3-4, on the other hand, formed a new $S_{adsorbate}$–$O_{surface}$ bond to generate an SO_4 unit on the surface in addition to new hydrogen bonds, resulting in adsorption energies ranging from –2.36 to –2.67 eV. These interactions are similar to those observed on the Al-terminated surface; no straightforward mechanism exists with which to dislodge the SO_4 from the surface without significantly altering the surface structure. H_2SO_3 and H_2SO_4 were again the adsorbates that interacted with the surface most strongly. In addition to the 3–7 hydrogen bonds present, the adsorbates were deprotonated by a surface hydroxyl group to form a H_2O molecule on the H-terminated surface. This process is akin to an acid-base reaction in which the alumina surface acts as the base, deprotonating sulfonic or sulfuric acid. All adsorption events on the H-terminated Al_2O_3 surface are depicted in Table S3 of the Supplemental Materials.

Table 1 Adsorption events on the Al-terminated alumina surface

Adsorbate	Configuration	E_{ads} (eV)	Interactions between surface and adsorbate
H_2S	1	–1.65	$Al_{surface}$–$S_{adsorbate}$ distance: 2.44 Å
H_2S	2	–2.34	H_2S deprotonated; Al–S bond length: 2.24 Å
SO_2	1	–2.10	$O_{absorbate}$ binds to surface; Al–O(S) bond length: 1.89 Å
SO_2	2	–1.98	$O_{adsorbate}$ binds to surface; Al–O(S) bond length: 1.89 Å
SO_3	1	–0.93	$O_{adsorbate}$ binds to surface; Al–O(S) bond length: 2.02 Å
SO_3	2	–3.50	$S_{adsorbate}$ binds to surface to form surface SO_4; new S–O(Al) bond length: 1.66 Å
SO_3	3	–3.50	$S_{adsorbate}$ binds to surface to form surface SO_4; new S–O(Al) bond length: 1.66 Å
SO_3	4	–3.49	$S_{adsorbate}$ binds to surface to form surface SO_4; new S–O(Al) bond length: 1.70 Å
H_2SO_3	1	–5.13	H–bonding (1); H_2SO_3 deprotonated
H_2SO_3	2	–4.05	H-bonding (1); H_2SO_3 deprotonated
H_2SO_4	1	–5.01	H-bonding (1); H_2SO_4 deprotonated
H_2SO_4	2	–4.43	H-bonding (1); H_2SO_4 deprotonated
H_2SO_4	3	–4.45	H-bonding (2); H_2SO_4 deprotonated

https://doi.org/10.1007/s42860-022-00194-5 Published online by Cambridge University Press

Table 2 Adsorption events on the H-terminated alumina surface

Adsorbate	Configuration	E_{ads} (eV)	Interactions between surface and adsorbate
H_2S	1	–1.78	H-bonding (3)
H_2S	2	–1.77	H-bonding (2)
SO_2	1	–1.11	H-bonding (2)
SO_2	2	–0.08	-
SO_3	1	–0.78	H-bonding (2)
SO_3	2	–0.08	H-bonding (1)
SO_3	3	–2.36	H-bonding (4); $S_{adsorbate}$ binds to surface to form surface SO_4; new S–O(Al) bond length: 1.73 Å
SO_3	4	–2.67	H-bonding (4); $S_{adsorbate}$ binds to surface to form surface SO_4; new S–O(Al) bond length: 1.82 Å
H_2SO_3	1	–3.75	H-bonding (7); H_2SO_3 deprotonated to form surface H_2O
H_2SO_3	2	–1.71	H-bonding (3)
H_2SO_4	1	–2.71	H-bonding (6); H_2SO_4 deprotonated to form surface H_2O
H_2SO_4	2	–2.50	H-bonding (4); H_2SO_4 deprotonated to form surface H_2O
H_2SO_4	3	–2.91	H-bonding (4); H_2SO_4 deprotonated to form surface H_2O

Al-terminated and H-terminated Alumina Surface Comparison

The adsorption energies calculated for the H-terminated surface were consistently less negative than the corresponding Al-terminated surface values. The only exception was H_2S-1. For both surface terminations, a clear trend was observed in which pollutants interact most strongly: H_2SO_4 is consistently the most detrimental adsorbate, with H_2SO_3 being just as harmful to the surface, albeit less consistently, as reflected by the magnitudes of their adsorption energies and number of hydrogen bonds and deprotonation events (Tables 1 and 2). With the exception of a few configurations, SO_3 formed SO_4 on both alumina surfaces, emphasizing the disruptive nature of SO_3 interacting with oxide surfaces. Although SO_2 and H_2S interacted significantly less with the alumina surfaces than the other adsorbates, they still formed non-negligible surface bonds. Overall, when exposed to this test set of sulfur-based adsorbates, both the Al-terminated and H-terminated alumina surfaces were likely to undergo undesirable surface transformations.

Although the strength of the interactions was consistently less on the H-terminated alumina surface, the nature of the interactions observed on the two surfaces were quite similar. For example, SO_3 was able to bind to the surface with the sulfur center adopting a tetrahedral geometry in both scenarios. This is depicted in Fig. 3, detailing the surface–adsorbate interactions present when Al- or H-terminated alumina was exposed to H_2SO_4-3. Both surfaces abstracted a proton from the adsorbate, but the resulting surface change was different, as a water molecule was formed on the H-terminated surface due to the already protonated surface. This example highlights the main difference between the two systems: the type of bond(s) formed between the adsorbate and surface is dictated by the surface termination. Specifically, Al–O bonds are formed on the Al-terminated surface, whereas the H-terminated surface can form only surface hydrogen bonds. The presence of protons on the surface hinders the attraction between the Al and O atoms by acting as a barrier on the surface.

Calcite ($CaCO_3$)

The calcite surface slab was created following the same methodology as the alumina surface. Bulk calcite was used to create a 2×2×1 supercell surface slab (Fig. 4). The calcite surface structure contained 120 atoms and has Ca–O bond lengths ranging from 2.30 to 2.55 Å and C–O bonds ranging from 1.27 to 1.32 Å. The corrugated complex of the surface can be seen in Fig. 4b, where the outer carbonates appear to be obtruding from the surface. A distinct layering pattern was seen in the surface structure, where the Ca cation layer alternates with the CO_3 layers. The H-terminated surface consisted of 124 atoms and differed from the Ca-terminated surface in its flat carbonate layers. It is depicted in Fig. S2 of the Supplemental Materials.

https://doi.org/10.1007/s42860-022-00194-5 Published online by Cambridge University Press

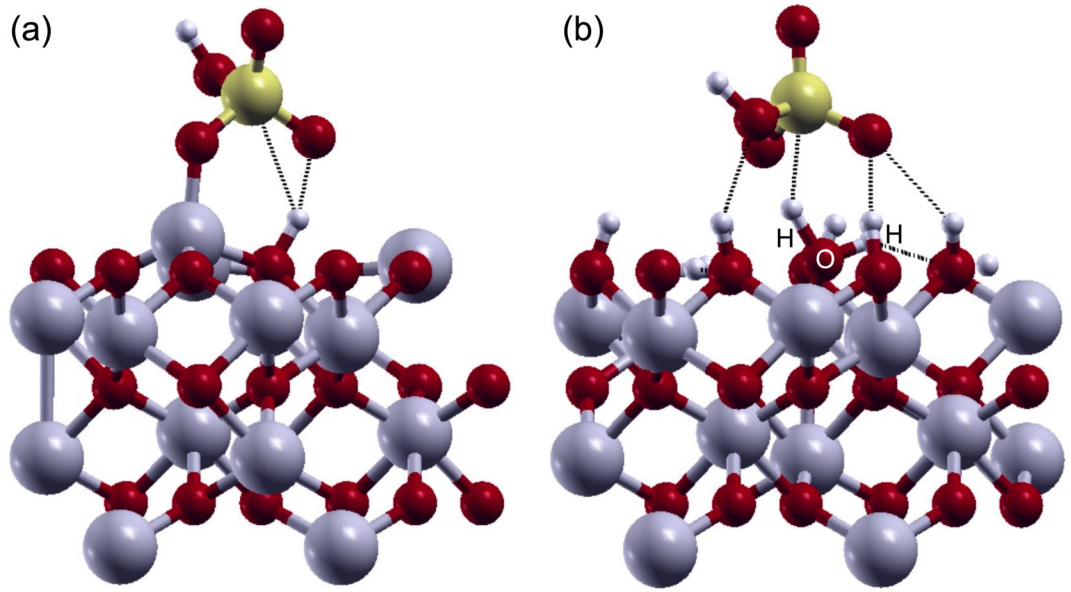

Fig. 3 Side view of the interactions between H_2SO_4-3 and an **a** Al-terminated or **b** H-terminated alumina surface. In b, the atoms of the H_2O molecule formed on the surface by deprotonation of sulfuric acid are labeled for clarity. Hydrogen and sulfur are shown as white and yellow spheres, respectively. Hydrogen bonds are represented by dotted black lines

Ca-terminated $CaCO_3$

As shown in Table 3, most configurations of the sulfur-based adsorbates tested here interacted strongly with the Ca-terminated calcite surface. The weakest interactions were observed with SO_2 and H_2S, which had adsorption energies ranging from –0.62 to –1.77 eV. The two configurations of H_2S formed identical structures on the surface, suggesting that H_2S will behave the same regardless of its initial orientation. In contrast, the resulting adsorption energy was dependent on the initial configuration of SO_2, as one of the orientations was able to form a Ca–O bond due to the proximity of one of the oxygen atoms of SO_2 facing toward the surface. This might explain why calcium sulfate growth from SO_2 on $CaCO_3$ has been shown to require O_3; it is very orientation-specific and requires additional oxidants (Zhang et al., 2018). All fully relaxed Ca-terminated

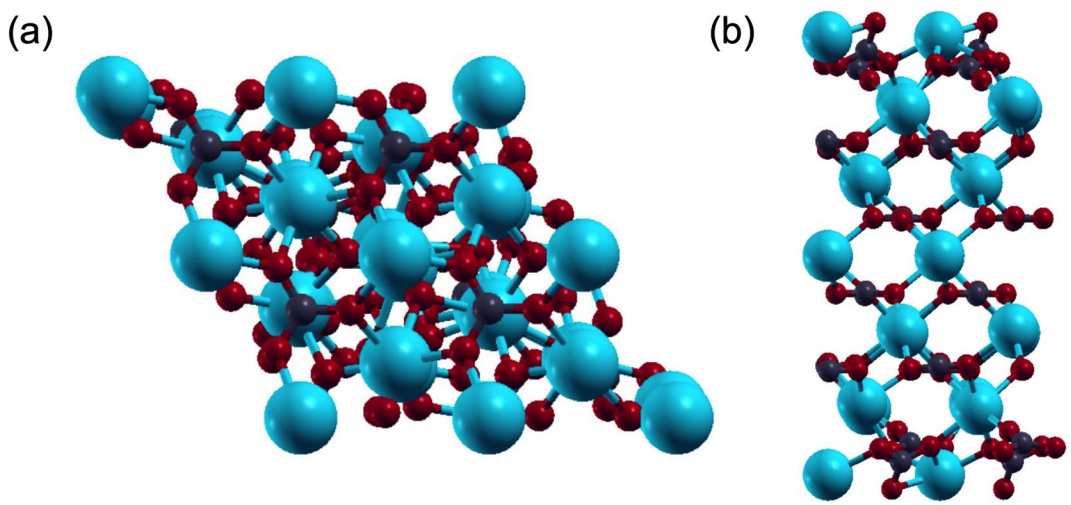

Fig. 4 **a** Top-down view along the 001 axis and **b** side view of the 2×2×1 calcite surface slab. Calcium, carbon, and oxygen atoms are represented as blue, black, and red spheres, respectively

https://doi.org/10.1007/s42860-022-00194-5 Published online by Cambridge University Press

Table 3 Adsorption events on the Ca-terminated calcite surface

Adsorbate	Configuration	E_{ads} (eV)	Interactions between surface and adsorbate
H_2S	1	-1.33	H-bonding (1); H_2S deprotonated
H_2S	2	-1.33	H-bonding (1); H_2S deprotonated
SO_2	1	-0.62	$S_{adsorbate}$-$O_{surface}$ distance: 2.19 Å
SO_2	2	-1.77	$O_{adsorbate}$ binds to surface; Ca-O(S) bond length: 2.28 Å
SO_3	1	-4.21	$S_{adsorbate}$ binds to surface to form surface SO_4; new S-O(Ca) bond length: 1.72 Å
SO_3	2	-3.29	$S_{adsorbate}$ binds to surface to form surface SO_4; new S-O(Ca) bond length: 1.80 Å
SO_3	3	-4.11	$S_{adsorbate}$ binds to surface to form surface SO_4; new S-O(Ca) bond length: 1.73 Å
SO_3	4	-2.48	$S_{adsorbate}$ binds to surface to form surface SO_4; new S-O(Ca) bond length: 1.73 Å
H_2SO_3	1	-3.35	H-bonding (1); H_2SO_3 deprotonated
H_2SO_3	2	-2.18	H-bonding (1); H_2SO_3 deprotonated
H_2SO_4	1	-3.34	H-bonding (1); H_2SO_4 deprotonated
H_2SO_4	2	-3.33	H-bonding (1); H_2SO_4 deprotonated
H_2SO_4	3	-2.98	H-bonding (2); H_2SO_4 deprotonated

$CaCO_3$ adsorption events are depicted in Table S4 of the Supplemental Materials.

SO_3, H_2SO_3, and H_2SO_4 all displayed significant bonding events with the Ca-terminated surface. For all configurations of SO_3, sulfur in its +6 oxidation state led to the formation of strong S–O(Ca) bonds, resulting in tetrahedral SO_4 molecules on the surface. This was similar to what was observed when SO_3 is exposed to MgO (Schneider et al., 2001) or when a mixture of SO_2 and O_2 is exposed to Al_2O_3 and CeO_2 (Smirnov et al., 2005). The example of the tetrahedral SO_4 unit formed is illustrated in Fig. 5a. H_2SO_3 and H_2SO_4 behaved quite similarly on the Ca-terminated calcite, as a proton was abstracted from the molecule in both cases. This behavior contributes to the thermodynamic favorability of these interactions, signifying the risk involved in sulfur-based pollutant exposure on the Ca-terminated calcite surface.

H-terminated $CaCO_3$

With the presence of hydrogen on the calcite surface, the strength of surface–adsorbate interactions decreased significantly. As seen by the minimal adsorption energies in Table 4, the H-terminated calcite surface appeared to be resilient against pollutant-promoted surface restructuring. In several cases, including SO_2, SO_3, and H_2SO_3, little to no interaction occurred, resulting in small (but still negative) adsorption energies ranging from –0.02 to –0.30 eV. Contrary to results presented earlier in this article, one configuration of H_2S displayed considerable interaction with the surface, resulting in an adsorption energy of –0.62 eV. Despite the overall weaker interactions observed with the other four adsorbates, the H-terminated calcite surface still interacted moderately with H_2SO_4, as indicated by adsorption energies ranging from –0.62 to –1.07 eV. Note that this is still significantly smaller than the adsorption energy calculations for H_2SO_4 on the other surfaces. This agrees with the hypothesis of the current work, that the presence of hydrogen combined with the flat, planar carbonates in the calcite structure creates a stable surface environment that discourages interactions with the set of sulfur-based adsorbates studied here. All adsorbate interaction on the H-terminated calcite surface are illustrated in Table S5 of the Supplemental Materials.

Ca-terminated and H-terminated Calcite Surface Comparison

There was a drastic difference in the interactions observed on the Ca-terminated and H-terminated calcite surfaces. Whereas the Ca-terminated surface was altered significantly when exposed to sulfur-based pollutants, the H-terminated surface appeared to be relatively unphased. An example of this dramatic difference is illustrated in Fig. 5, which shows how a specific configuration of SO_3 differed in its bonding across the two surfaces. On the Ca-terminated surface, the adsorbate is completely ingrained into the surface structure, as the

https://doi.org/10.1007/s42860-022-00194-5 Published online by Cambridge University Press

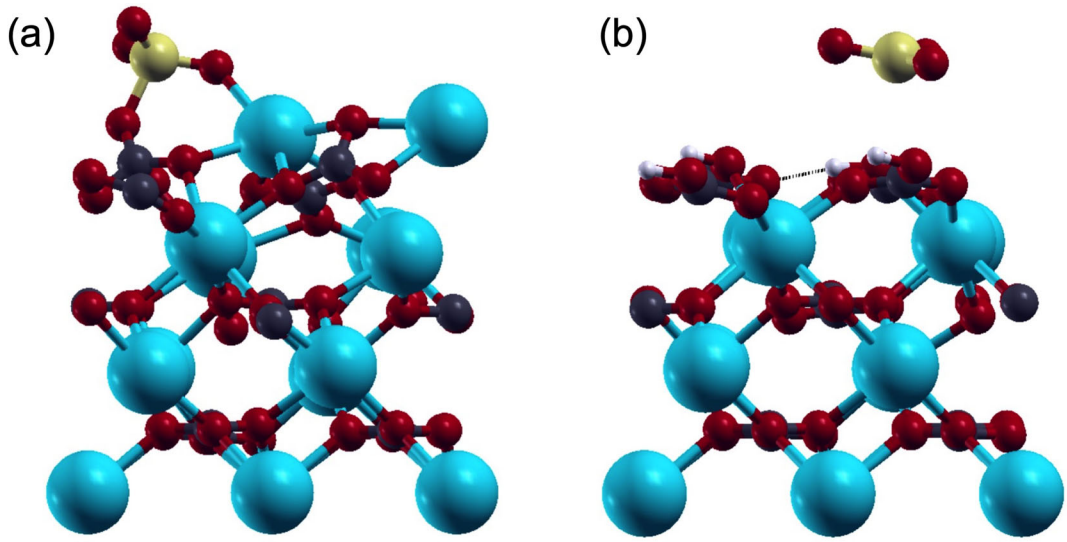

Fig. 5 Side view of **a** Ca-terminated and **b** H-terminated calcite surface when exposed to SO_3-3. Same color schemes as in previous figures

central sulfur bonds to a carbonate group and the adsorbate oxygen bonds to a surface calcium atom. In contrast, on the H-terminated surface, SO_3 displays no bonding events and simply hovers above the surface. This trend was observed across most of the adsorbates tested; the adsorbates interacted strongly with the Ca-terminated calcite surface but did not do so on the H-terminated surface. One possible explanation for this discrepancy could be the inherent stability of the layered carbonate structure on the calcite surface. After adding protons to the calcite surface, the carbonates on the calcite surface transition from being corrugated to a planar structure. As a result, the structure becomes less susceptible to pollutant-promoted restructuring.

Discussion

The alumina surface exhibited more substantial interactions with this test set of sulfur-based adsorbates than its calcite counterpart. In Fig. 6, where the dashed line represents a one-to-one correlation between the E_{ads} on the metal- and H-terminated surfaces, points above the line signify that a given adsorbate interacts

Table 4 Adsorption events on the H-terminated calcite surface

Adsorbate	Configuration	E_{ads} (eV)	Interactions between surface and adsorbate
H_2S	1	–0.62	H-bonding (2)
H_2S	2	–0.11	H-bonding (1)
SO_2	1	–0.19	H-bonding (1)
SO_2	2	–0.12	-
SO_3	1	–0.30	-
SO_3	2	–0.02	-
SO_3	3	–0.27	-
SO_3	4	–0.30	-
H_2SO_3	1	–0.04	-
H_2SO_3	2	–0.07	-
H_2SO_4	1	–1.07	H-bonding (2)
H_2SO_4	2	–0.62	H-bonding (1)
H_2SO_4	3	–0.88	H-bonding (2)

https://doi.org/10.1007/s42860-022-00194-5 Published online by Cambridge University Press

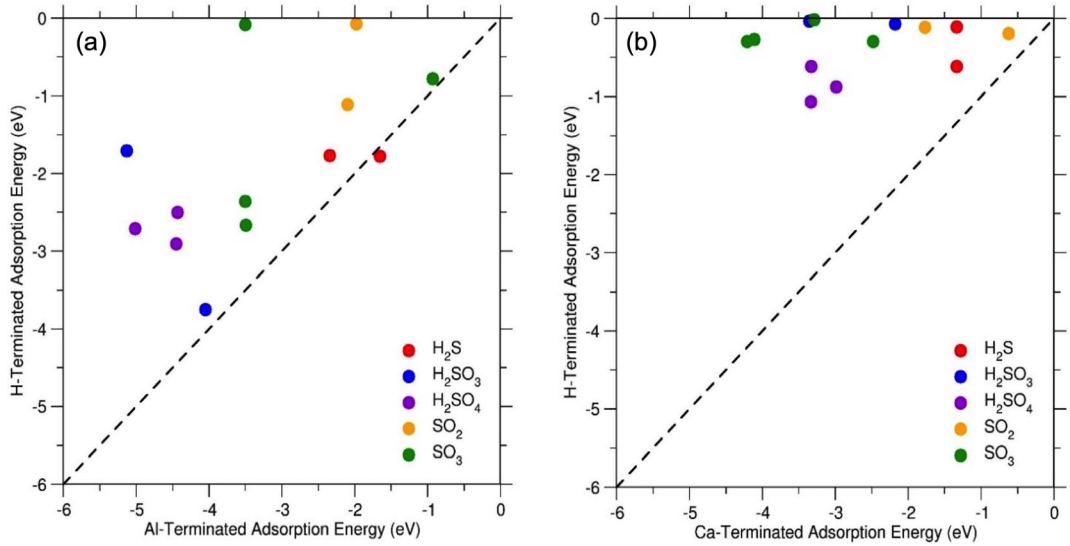

Fig. 6 Correlation plots for all adsorbates and configurations on the **a** alumina or **b** calcite surfaces. Each point represents a particular adsorbate and configuration. A one-to-one correlation between the calculated E_{ads} on the metal- and H-terminated surface is represented by the dotted line. Points above the dotted line indicate that a more negative adsorption energy was observed on the metal-terminated surface. H_2S is represented in red, SO_2 in orange, SO_3 in green, H_2SO_3 in blue, and H_2SO_4 in purple

with the metal-terminated surface more strongly, while points below indicate a more negative adsorption energy on the H-terminated surface. As seen in Fig. 6b, all adsorption energies were several times greater (more negative) on the Ca-terminated calcite surface compared to the H-terminated surface. Apart from two configurations of SO_3, stronger or equal interactions were observed on the Al-terminated alumina surface when compared to the Ca-terminated calcite surface. This gap is further widened when comparing the H-terminated alumina surface to the H-terminated calcite surface. Whereas the H-terminated alumina surface exhibited sizable interactions with most adsorbates, the H-terminated calcite surface was barely influenced by the presence of the adsorbates. Figure 6 also illustrates how adsorption energies vary significantly based on the initial orientation of the adsorbates. For example, there is a large distance between the two blue H_2SO_3 points in Fig. 6a, signifying a configuration-dependent difference in resulting interactions among the two configurations on the alumina surface. A larger disparity can be seen in one configuration of SO_3 on the alumina surface. On the other hand, the adsorption energy of H_2SO_4 appears relatively independent of initial orientation, as the value does not fluctuate significantly between configurations.

The significant role that the orientation of the adsorbate often plays in the interactions observed in the final structure is explored in Fig 7. Each column in Fig. 7 signifies a specific adsorbate and surface, and as shown, the interactions between the adsorbates and surfaces vary significantly based on the initial orientation parameters. For example, SO_3-1 was positioned vertically on the surface, while SO_3-2 was positioned flat, both over a surface Al atom (Fig. 7a). The resulting structures differ in terms of both the distance and the number of bonds formed between surface and adsorbate; the flat SO_3 was able to anchor itself into the surface to form a tetrahedral SO_4, while the vertically oriented SO_3 formed only a (S)O–Al interaction. Furthermore, as seen in Fig. 7c, a simple rotation in the initial orientation of H_2SO_3 produces a system with a deprotonation event, four additional hydrogen bonds, and an adsorption energy greater (more negative) in magnitude by 2.04 eV. Similar patterns are depicted in Fig. 7b and d, where the initial configurations determined whether an S–O(Al) bond (7b) or a second (S)O–Ca bond was formed (7d). These drastic differences suggest that not only does surface material and adsorbate type affect the resulting interactions, but the initial orientation plays a significant role as well.7

Across all surface–adsorbate systems, clear trends in the impact of each adsorbate were visible. First, the strength of the interactions tended to increase as adsorbate molecule size increased. As seen in Fig. 6a and b, H_2S and SO_2 consistently resulted in the least negative adsorption energies, regardless of the surface model.

https://doi.org/10.1007/s42860-022-00194-5 Published online by Cambridge University Press

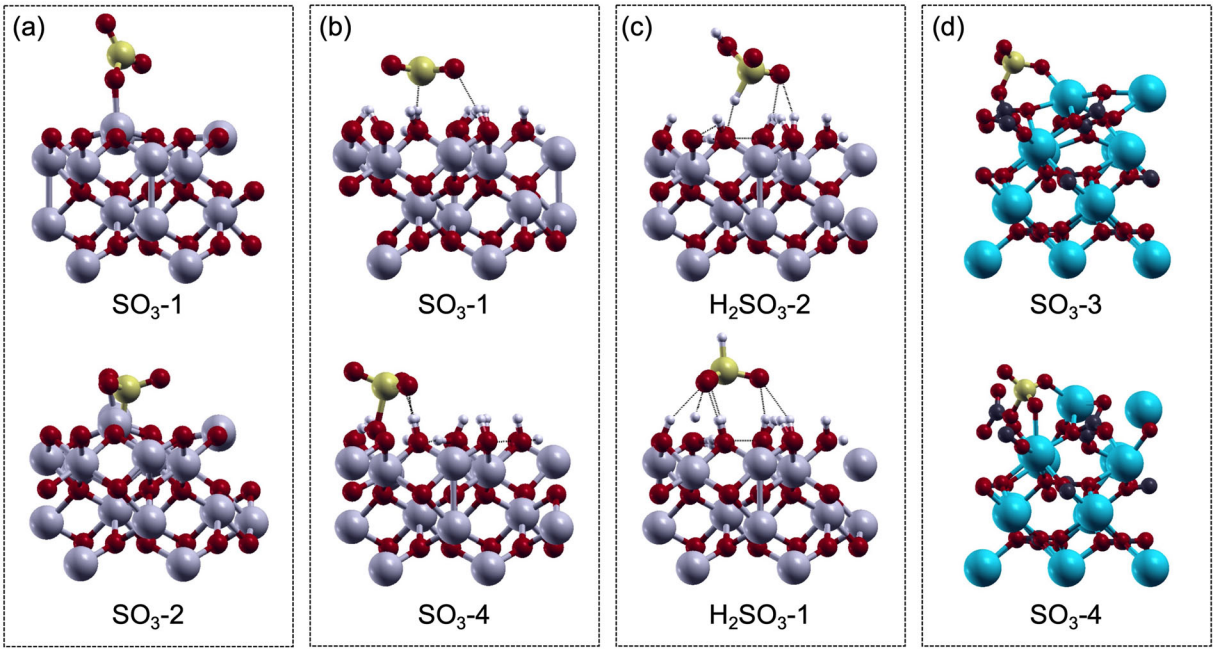

Fig. 7 Side views of various structures to compare the effect of initial orientation on the resulting surface-adsorbate interactions. **a** SO_3 on Al-terminated alumina surface, **b** SO_3 on H-terminated alumina surface, **c** H_2SO_3 on H-terminated alumina surface, and **d** SO_3 on Ca-terminated calcite surface. Same color scheme as in previous figures

Subsequently, H_2SO_3 and SO_3 appear to have surface–adsorbate interactions that are comparable in magnitude but are more variable than H_2SO_4. Across all surfaces investigated here, H_2SO_4 stands out as the most potentially destructive molecule. To illustrate this effect, H_2SO_4 adsorption energies (purple dots) clustered to the left of most other adsorbates (Fig. 6). Each surface structure after exposure to H_2SO_4 is showcased in Fig. 8. H_2SO_4 has the greatest contact area and thus can exhibit more bonding events with the surface. The presence of protons on the molecule also enabled basic oxide-based surfaces to deprotonate the adsorbate, further contributing to a negative adsorption energy. Differences in surface structure and composition were also shown to influence the interactions observed with H_2SO_4 (Fig. 8). For example, a notable contrast was seen between the interactions shown in Fig. 8b and Fig. 8d. The H-terminated alumina (Fig. 8b) was able to deprotonate H_2SO_4 and form four hydrogen bonds, while H_2SO_4 only forms two hydrogen bonds to the

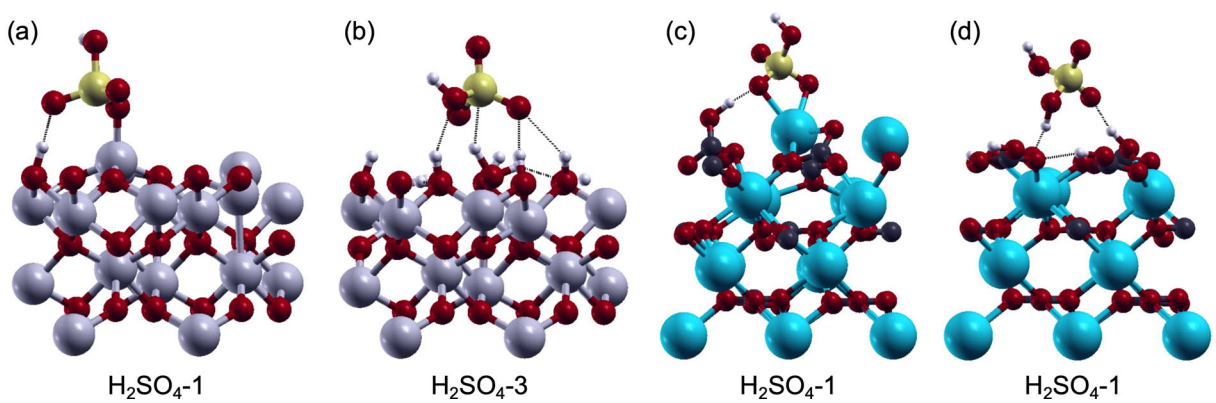

Fig. 8 Side view of the interactions between H_2SO_4 and **a** Al-terminated alumina surface, **b** H-terminated alumina surface, **c** Ca-terminated calcite surface, and **d** H-terminated calcite surface. Each structure showcases the H_2SO_4 configuration that resulted in the most negative adsorption energy for that specific surface

https://doi.org/10.1007/s42860-022-00194-5 Published online by Cambridge University Press

H-terminated calcite with no other interactions present (Fig. 8d). This disparity in the type and magnitude of interactions on the alumina versus calcite surfaces can be explained by slight differences in their crystal structure. While these materials have similar structures, the surface calcium in calcite is shielded by a carbon atom (carbonate group) above it. The effects of this protective layer are seen in both the Ca- and H-terminated surfaces. As a result, calcite surfaces were less prone to bonding with sulfur-based molecules. The impact that surface hydrogens have on preventing or minimizing covalent surface–adsorbate interactions is also illustrated in Fig. 8. Whereas robust covalent bonds can form on the metal-terminated surfaces, only hydrogen bonding occurs on the H-terminated surfaces. The hydrogen atoms serve as a barrier protecting the metal cations on the surface from the adsorbates.

Conclusion

The present study provides an atomistic picture of the vulnerabilities of oxide-mineral surfaces to sulfur-based pollutants. Calcite and alumina are two oxide minerals that are potentially prone to surface disruptions caused by sulfur-based small molecules, but their range of surface–adsorbate interactions had not yet been fully compared. To correlate how these mineral oxides with similar crystallographic features responded to sulfur-based adsorbates, a DFT investigation of their surface interactions with H_2S, SO_2, SO_3, H_2SO_3, and H_2SO_4 was conducted. Under vacuum conditions, the adsorbates were anchored to the metal-terminated calcite and alumina (001) surfaces, resulting in substantial (negative) adsorption energies and a number of bonding events. These considerably large negative adsorption energies were due to the formation of metal–oxygen bonds on the surface, changes in local symmetry, and the creation of hydrogen-bonding networks. Under atmospheric conditions, where the surfaces are protonated, interactions tended to decrease, but were still sizeable for H-terminated alumina. The surface interactions modeled here will precede any inner-sphere adsorptions and, on a large scale (or over time), might be responsible for deteriorating surface integrity, thus severely undermining infrastructural stability in building materials containing alumina. In contrast, most of the interactions observed on the H-terminated calcite surface were practically negligible. This contrast might be explained by both orientation effects of the flat, unreactive carbonate group in calcite and its location directly over the more reactive Ca atoms; the carbonate and bicarbonate anion effectively shielded subsurface Ca atoms from adsorption events. Due to the resilient nature of the calcite surface, there might be a greater urgency in identifying methods to protect alumina surfaces from sulfur-based pollutants.

Also highlighted here is the role that orientation effects of sulfur-based molecules have on the resulting surface–adsorbate systems. Drastic differences in adsorption energy were observed, and bonding events could be attributed directly to the starting orientation of the adsorbate. Interestingly, the configuration-dependent changes in E_{ads} are more significant for larger molecules as opposed to smaller molecules. The importance of the oxidation state of sulfur in these various compounds must also not be overlooked. For oxide-based materials, the difference in electronegativity between oxygen and the metal, coupled with atomistic geometry, determines the strength of the bond exhibited on the surface. This factor explains why trigonal planar SO_3 often bonds to the surface to form tetrahedral SO_4, while SO_2 does not.

The work performed here on adsorbates serves as an atomistic starting point for more advanced analyses that include: (1) ab initio molecular dynamics (Iftimie et al., 2005; Kresse & Hafner, 1993) to sample more local adsorption configurations: (2) atom-centered basis sets like the DMol3 package to sample larger supercells; (3) variable solvation, either explicitly or implicitly using methods like the COSMO model (Klampt & Schuurmann, 1993); and (4) inner-sphere adsorption processes where a surface water is displaced by a ligand attaching to a surface. These extensions would help to understand better the possible mechanisms of complex adsorption processes with multiple adsorbates and how the hydrogen bonding surface networks would be affected by aqueous media. Using the recently developed DFT + Solvent Ion method, the exchange of surface metals for protons in an aqueous environment was predicted to be favorable for a wide range of pH values for both the (001) surfaces of calcite and alumina. Extending these calculations to include anion and cation release from a surface would allow for the investigation of defect structures and the pH values at which they form to ascertain the effects of adsorbate behavior in the presence of acid rain (Bennett et al., 2018; Grimes et al., 2021; Rong & Kolpak, 2015). Building upon this, these calculations could also include

https://doi.org/10.1007/s42860-022-00194-5 Published online by Cambridge University Press

different cations via sulfate salts and more complex mixed cation/anion compositions to map out how tuning chemical environments could mimic sulfate-fouled carbonate surfaces, assist in mineral dissolution, or be used to create potentially sulfur-repellant surfaces (Chong & Sheikholeslami, 2001; Cubillas et al., 2005; Lea et al., 2001; Sheikholeslami & Ng, 2001). Additionally, the (001) surfaces of alumina and calcite are not the only ones encountered in nature and under synthesis conditions; the structures of the $(10\bar{1}4)$ surface of calcite (Fenter et al., 2013) and the $(1\bar{1}02)$ surface of alumina (Mason et al., 2010) have been examined previously across a wide range of mineral-surface reactivity studies.

The specific atomistic information collected here and in subsequent analyses will facilitate the identification of specific structural properties that are reactive to adsorption. For example, the protonated calcite surface featured a flat carbonate layer which can prevent adsorption events by blocking the subsurface Ca ions. This information can be used to manufacture materials that are resistant to sulfur-based adsorbates as well as evaluate the functionality of the material in catalysis and as a sensor for gas detection (Breedon et al., 2010; Weijing et al., 2018). The subsequent steps in this process involve translating the theoretical observations into an experimental setting to observe interactions on a macro-scale and identify solutions to protect oxide-based surfaces from sulfur-based pollutants, with direct applications in mineral weathering, acid mine drainage, CO_2 release from carbonaceous minerals, and desalination membrane fouling (Mayorga et al., 2018; Rodriguez et al., 2000; Torres et al., 2018; Warsinger et al., 2015; Zeebe et al., 2008).

Supplementary Information The online version contains supplementary material available at https://doi.org/10.1007/s42860-022-00194-5.

Acknowledgments J. E. H. is supported by the Andrew W. Mellon Foundation under Award 41500634. Additional funding for the computational program was provided by the Extreme Science and Engineering Discovery Environment (XSEDE)[59] start-up grant TG-CHE190075 and renewal allocation TG-CHE200108, which are supported by National Science Foundation grant number ACI-1548562. Some calculations were performed using the UMBC High Performance Computing Facility (HPCF). The acquisition of equipment for the UMBC HPCF is partially supported by the National Science Foundation (the support of which is acknowledged gratefully), and which requires the following notice: This material is based upon work supported by the National Science Foundation under the MRI grants CNS-0821258, CNS-1228778, and OAC-1726023, and the SCREMS grant DMS-0821311. The atomistic images in this work were generated using *XCrySDen*.

Author's Contributions SO performed calculations, created figures, prepared the manuscript and supplemental materials; JEH outlined calculations, prepared and edited the manuscript and supplemental materials; JWB outlined project scope, prepared and edited the manuscript and supplemental materials.

Funding J. E. H. is supported by the Andrew W. Mellon Foundation under Award 41500634.

Data Availability Structural relaxation data can be provided upon reasonable request.Supplementary Information The online version contains supplementary material available at https://doi.org/10.1007/s42860-022-00194-5.

Code Availability Not applicable, *Quantum ESPRESSO* and *XCrysden* are open-source codes.Supplementary Information The online version contains supplementary material available at https://doi.org/10.1007/s42860-022-00194-5.

Declarations

Conflict of Interest The authors declare no conflict of interest or competing interest.

References

Abbaspour-Tamijani, A., Bjorklund, J. L., Augustine, L. J., Catalano, J. G., & Mason, S. E. (2020). Density functional theory and thermodynamics modeling of inner-sphere oxyanion adsorption on the hydroxylated alpha-Al_2O_3 (001) Surface. *Langmuir, 36*(44), 13166–13180.

Baltrusaitis, J., Cwiertny, D. M., & Grassian, V. H. (2007). Adsorption of sulfur dioxide on hematite and goethite particle surfaces. *Physical Chemistry Chemical Physics, 9*(41), 5542. https://doi.org/10.1039/b709167b

Baltrusaitis, J., Jayaweera, P. M., & Grassian, V. H. (2010). Sulfur dioxide adsorption on TiO_2 nanoparticles: Influence of particle size, co-adsorbates, sample pretreatment, and light on SURFACE speciation and surface coverage. *The Journal of Physical Chemistry C, 115*(2), 492–500.

Bennett, J. W., Bjorklund, J. L., Forbes, T. Z., & Mason, S. E. (2017). Systematic study of aluminum nanoclusters and anion adsorbates. *Inorganic Chemistry, 56*, 13014–13028.

Bennett, J. W., Jones, D., Huang, X., Hamers, R. J., & Mason, S. E. (2018). Dissolution of complex metal oxides from first-principles and thermodynamics: Cation removal from the (001) surface of $Li(Ni_{1/3}Mn_{1/3}Co_{1/3})O_2$. *Environmental Science & Technology, 52*(10), 5792–5802.

Bennett, J. W., Jones, D. T., Hudson, B. G., Melendez-Rivera, J., Hamers, R. J., & Mason, S. E. (2020). First-principles and thermodynamics comparison of compositionally-tuned delafossites: Cation release from the (001) surface of

https://doi.org/10.1007/s42860-022-00194-5 Published online by Cambridge University Press

complex metal oxides. *Environmental Science: Nano, 7*, 1642–1651.

Bjorklund, J. L., Bennett, J. W., Forbes, T. Z., & Mason, S. E. (2019). Modeling of MAl_{12} Keggin heteroatom reactivity by anion adsorption. *Crystal Growth & Design, 19*, 2820–2829.

Bravo, A. H., Soto, A. R., Sosa, E. R., Sanchez, A. P., Alarcon, J. A. L., Kahl, J., & Ruiz, B. J. (2006). Effect of acid rain on building material of the El Tajin archaeological zone in Veracruz, Mexico. *Environmental Pollution, 144*, 655–660.

Breedon, M., Spencer, M. J., & Yarovsky, I. (2010). Adsorption of NO_2 on oxygen deficient ZnO($2\bar{1}\bar{1}0$) for Gas Sensing Applications: A DFT study. *The Journal of Physical Chemistry C, 114*(39), 16603–16610. https://doi.org/10.1021/jp105733p

Bridges, A., Felder, F. A., McKelvey, K., & Niyogi, I. (2015). Uncertainty in energy planning: Estimating the health impacts of air pollution from fossil fuel electricity generation. *Energy Research & Social Science, 6*, 74–77.

Burke, K. (2012). Perspective on density functional theory. *The Journal of Chemical Physics, 136*(15), 150901. https://doi.org/10.1063/1.4704546

Chessin, H., Hamilton, W. C., & Post, B. (1965). Position and thermal parameters of oxygen atoms in calcite. *Acta Crystallographica, 18*, 689–693.

Chong, T. H., & Sheikholeslami, R. (2001). Thermodynamics and kinetics for mixed calcium carbonate and calcium sulfate precipitation. *Chemical Engineering Science, 56*, 5391–5400.

Coccato, A., Moens, L., & Vandenabeele, P. (2017). On the Stability of Mediaeval Inorganic Pigments: A Literature Review of the Effect of Climate, Material Selection, Biological Activity, Analysis and Conservation Treatments. *Heritage Science, 5*(1), 12.

Corum, K. W., Huang, X., Bennett, J. W., & Mason, S. E. (2017). Systematic Density Functional Theory Study of the Structural and Electronic Properties of Constrained and Fully Relaxed (001) Surfaces of Alumina and Hematite. *Molecular Simulation, 43*(5-6), 406–419.

Cubillas, P., Kohler, S., Prieto, M., Chairat, C., & Oelkers, E. H. (2005). Experimental determination of the dissolution rates of calcite, aragonite, and bivalves. *Chemical Geology, 216*, 59–77.

Fenger, J. (1999). Urban air quality. *Atmospheric Environment, 33*, 4877–4900.

Fenter, P., Kerisit, S., Raiteri, P., & Gale, J. D. (2013). Is the Calcite-Water Interface Understood? *Direct Comparisons of Molecular Dynamics Simulations with Specular X-ray Reflectivity Data. The Journal of Physical Chemistry C., 117*, 5028–5042.

Galloway, B. D., Sasmaz, E., & Padak, B. (2015). Binding of SO_3 to fly ASH components: CaO, MgO, Na_2O and K_2O. *Fuel, 145*, 79–83. https://doi.org/10.1016/j.fuel.2014.12.046

Garcia-Florentino, C., Maguregui, M., Carrero, J. A., Morillas, H., Arana, G., & Madariaga, J. M. (2020). Development of a cost effective passive sampler to quantify the particulate matter depositions on building materials over time. *Journal of Cleaner Production, 268*, 122134–121-10.

Garrity, K. F., Bennett, J. W., Rabe, K. M., & Vanderbilt, D. (2014). Pseudopotentials for High-Throughput DFT Calculations. *Computational Materials Science, 81*, 446–452. https://doi.org/10.1016/j.commatsci.2013.08.053

Gettens, R. J., Fitzhugh, E. W., & Feller, R. L. (1974). Calcium Carbonate Whites. *Studies in Conservation, 19*(3), 157–184.

Giannozzi, P., Baroni, S., Bonini, N., Calandra, M., Car, R., Cavazzoni, C., Ceresoli, D., Chiarotti, G. L., Cococcioni, M., Dabo, I., Dal Corso, A., de Gironcoli, S., Fabris, S., Fratesi, G., Gebauer, R., Gerstmann, U., Gougoussis, C., Kokalj, A., Lazzeri, M., … Wentzcovitch, R. M. (2009). Quantum Espresso: A modular and open-source software project for quantum simulations of materials. *Journal of Physics: Condensed Matter, 21*(39), 395502. https://doi.org/10.1088/0953-8984/21/39/395502

Graue, B., Siegesmund, O. P., Naumann, R., Licha, T., & Simon, K. (2013). The effect of air pollution on stone decay: The decay of the Drachenfels trachyte in industrial, urban, and rural environments – A case study of the Cologne, Altenberg and Xanten cathedrals. *Environmental Earth Sciences, 69*, 1095–1124.

Grimes, R. T., Leginze, J. A., Zochowski, R., & Bennett, J. W. (2021). Surface transformations of lead oxides and carbonates using first-principles and thermodynamics calculations. *Inorganic Chemistry, 60*(2), 1228–1240. https://doi.org/10.1021/acs.inorgchem.0c03398

Gulia, S., Shiva Nagendra, S. M., Khare, M., & Khanna, I. (2015). Urban air quality management – A review. *Atmospheric Pollution Research, 6*, 286–304.

Gunasekaran, S., & Anbalagan, G. (2007). Spectroscopic characterization of natural calcite minerals. *Spectrochimica Acta Part A: Molecular and Biomolecular Spectroscopy, 68*(3), 656–664. https://doi.org/10.1016/j.saa.2006.12.043

He, K., Song, Q., Yan, Z., & Yao, Q. (2020). SO_3 removal from flue gas by using Na_2SO_3. *Energy & Fuels, 34*(6), 7232–7241. https://doi.org/10.1021/acs.energyfuels.0c00476

He, K., Song, Q., Yan, Z., Zheng, N., & Yao, Q. (2019). Study on competitive absorption of SO_3 and SO_2 by calcium hydroxide. *Fuel, 242*, 355–361. https://doi.org/10.1016/j.fuel.2019.01.046

Heimann, J. E., Grimes, R. T., Rosenzweig, Z., & Bennett, J. W. (2021). A density functional theory (DFT) investigation of how small molecules and atmospheric pollutants relevant to art conservation adsorb on kaolinite. *Applied Clay Science, 206*, 106075. https://doi.org/10.1016/j.clay.2021.106075

Hellenbrandt, M. (2004). The Inorganic Crystal Structure Database (ICSD) – present and future. *Crystallography Reviews, 10*(1), 17–22. https://doi.org/10.1080/08893110410001664882

Hosseinabad, E. R., & Moraga, R. J. (2017). A system dynamics approach in air pollution mitigation of metropolitan areas with sustainable development perspective: A case study of Mexico City. *Journal of Applied Environmental and Biological Sciences, 7*(12), 164–174.

Huang, X., Bennett, J. W., Hang, M. N., Laudadio, E. D., Hamers, R. J., & Mason, S. E. (2017). Ab initio atomistic thermodynamics study of the (001) surface of $LiCoO_2$ in a water environment and implications for reactivity under ambient conditions. *The Journal of Physical Chemistry C, 121*(9), 5069–5080. https://doi.org/10.1021/acs.jpcc.6b12163

Iftimie, R., Minary, P., & Tuckerman, M. E. (2005). Ab initio molecular dynamics: Concepts, recent developments, and future trends. *Proceedings of the National Academy of Sciences, 102*(19), 6654–6659.

Klampt, A., & Schuurmann, G. (1993). COSMO: A new approach to dielectric screening in solvents with explicit expressions

https://doi.org/10.1007/s42860-022-00194-5 Published online by Cambridge University Press

for the screening energy and its gradient. *Journal of the Chemical Society, Perkin Transactions, 2*(5), 799–805.

Kohn, W., & Sham, L. J. (1965). Self-consistent equations including exchange and correlation effects. *Physical Review, 140*(4A). https://doi.org/10.1103/physrev.140.a1133

Kokalj, A. (1999). XcrySDen—a new program for displaying crystalline structures and electron densities. *Journal of Molecular Graphics and Modelling, 17*(3-4), 176–179. https://doi.org/10.1016/s1093-3263(99)00028-5

Kresse, G., & Hafner, J. (1993). *Ab initio* molecular dynamics for liquid metals. *Physical Review B, 47*, 558I.

Lea, A. S., Amonette, J. E., Baer, D. R., Liang, Y., & Colton, N. G. (2001). Microscopic effects of carbonate, manganese, and strontium ions on calcite dissolution. *Geochimica et Cosmochimica Acta, 65*(3), 369–379.

Lim, C. C., Kim, H., Ruzmyn Vilcassim, M. J., Thurston, G. D., Gordon, T., Chen, L.-C., Lee, K., Heimbinder, M., & Kim, S.-Y. (2019). Mapping urban air quality using mobile sampling with low-cost sensors and machine learning in Seoul, South Korea. *Environment International, 131*, 105022–101-10.

Liu, D., Jin, Y., & Deng, J. (2009). Ab initio calculations of the relationship between the alpha alumina toughness and its electronic structure under pressure. *Computational Materials Science, 45*(2), 310–314. https://doi.org/10.1016/j.commatsci.2008.10.002

Martins, F., Felgueiras, C., Smitkova, M., & Caetano, N. (2019). Analysis of fossil fuel energy consumption and environmental impacts in European countries. *Energies, 12*, 964–1-11.

Mason, S. E., Iceman, C. R., Trainor, T. P., & Chaka, A. M. (2010). Density functional theory study of clean, hydrated, and defective alumina (11\bar02) surfaces. *Physical Review B, 81*, 125423–121-16.

Mayorga, I. C., Astilleros, J. M., Fernando-Diaz, L., Morales, J., Prieto, M., Roncal-Herrero, T., & Benning, L. G. (2018). Epitactic Overgrowths of Calcite ($CaCO_3$) on Anhydrite ($CaSO_4$) Cleavage Surfaces. *Crystal Growth & Design, 18*, 1666–1675.

Perera, F. P. (2017). Multiple threats to child health from fossil fuel combustion: Impacts of air pollution and climate change. *Environmental Health Perspectives, 125*(2), 141–148.

Rodriguez, J. A., Jirsak, T., Freitag, A., Larese, J. Z., & Maiti, A. (2000). Interaction of SO_2 with MgO (100) and Cu/Mg (100): Decomposition reactions and formation of SO_3 and SO_4. *The Journal of Physical Chemistry B, 104*, 7439–7448.

Rong, X., & Kolpak, A. M. (2015). *Ab initio* approach for prediction of oxide surface structure, stoichiometry, and electrocatalytic activity in aqueous solution. *Journal of Physical Chemistry Letters., 6*(9), 1785–1789.

Schneider, W. F., Li, J., & Hass, K. C. (2001). Combined computational and experimental investigation of SO_x Adsorption on MgO. *The Journal of Physical Chemistry B, 105*, 6972–6979.

Shannon, R. D., & Prewitt, C. T. (1969). Effective ionic radii in oxides and fluorides. *Acta Crystallographica Section B Structural Crystallography and Crystal Chemistry, 25*(5), 925–946. https://doi.org/10.1107/s0567740869003220

Sheikholeslami, R., & Ng, M. (2001). Calcium sulfate precipitation in the prescence of nondominant calcium carbonate: Thermodynamics and kinetics. *Industrial & Engineering Chemistry Research, 40*, 3570–3578.

Smirnov, M. Y., Kalinin, A. V., Pashis, A. V., Sorokin, A. M., Noskov, A. S., Kharas, K. C., & Bukhtiyarov, V. I. (2005). Interaction of Al_2O_3 and CeO_2 surfaces with SO_2 and SO_2 + O_2 Studied by X-ray Photoelectron Spectroscopy. *The Journal of Physical Chemistry B., 109*, 11712–11719.

Summers, J. C. (1979). Reaction of sulfur oxides with alumina and platinum/alumina. *Environmental Science & Technology, 13*(3), 341–345.

Toebbens, D. M., Stuessaer, N., Knorr, K., Mayer, H. M., & Lampert, G. (2001). The new high-resolution neutron powder diffractometer at the Berlin neutron scattering center. *Materials Science Forum., 378*, 288–293. https://doi.org/10.4028/www.scientific.net/MSF.378-381.288

Torres, E., Lozano, A., Macias, F., Gomez-Arias, A., & Castillo, J. (2018). Passive elimination of sulfate and metals from acid mine drainage using combined limestone and barium carbonate systems. *Journal of Cleaner Production, 182*, 114–123.

Warsinger, D. M., Swaminathan, J., Guillen-Burrieza, E., Arafat, H. A., & Lienhard, J. H. (2015). Scaling and fouling in membrance distillation for desalination applications: A review. *Desalination, 356*, 294–313.

Weijing, D., Weihong, Z., Xiaodong, Z., Baofeng, Z., Lei, C., Laizhi, S., Shuangxia, Y., Haibin, G., Guanyi, C., Liang, Z., & Ge, S. (2018). The application of DFT in catalysis and adsorption reaction system. *Energy Procedia, 152*, 997–1002. https://doi.org/10.1016/j.egypro.2018.09.106

Wilkins, R. G. (1991). *Kinetics and Mechanism of Reactions of Transition Metal Complexes*. Allyn & Bacon, Inc..

Wu, Z., & Cohen, R. E. (2006). More accurate generalized gradient approximation for solids. *Physical Review B, 73*(23). https://doi.org/10.1103/physrevb.73.235116

Yao, L., Fan, X., Yan, C., Kurtén, T., Daellenbach, K. R., Li, C., Wang, Y., Guo, Y., Dada, L., Rissanen, M. P., Cai, J., Tham, Y. J., Zha, Q., Zhang, S., Du, W., Yu, M., Zheng, F., Zhou, Y., Kontkanen, J., … Bianchi, F. (2020). Unprecedented ambient sulfur trioxide (SO_3) detection: Possible formation mechanism and atmospheric implications. *Environmental Science & Technology Letters, 7*(11), 809–818. https://doi.org/10.1021/acs.estlett.0c00615

Zeebe, R. E., Zachos, J. C., Caldeira, K., & Tyrell, T. (2008). Carbon Emissions and Acidification. *Science, 321*, 51–52.

Zhang, Y., Tong, S., Ge, M., Jing, B., Hou, S., Tan, F., Chen, Y., Guo, Y., & Wu, L. (2018). The formation and growth of calcium sulfate crystals through oxidation of SO_2 by O_3 on size-resolved calcium carbonate. *The Royal Society of Chemistry Advances, 8*, 16285.

Zheng, C., Wang, Y., Liu, Y., Yang, Z., Qu, R., Ye, D., Liang, C., Liu, S., & Gao, X. (2019). Formation, transformation, measurement, and control of SO_3 in coal-fired power plants. *Fuel, 241*, 327–346.

https://doi.org/10.1007/s42860-022-00194-5 Published online by Cambridge University Press